# Passive control of wall shear stress and mass transfer generated by submerged lobed impinging jet

Kodjovi Sodjavi, Brice Montagné, Amina Meslem, Paul Byrne, Laurent Serres, Vaclav Sobolik

# Passive control of wall shear stress and mass transfer generated by submerged lobed impinging jet

Kodjovi Sodjavi[1], Brice Montagné[1], Amina Meslem[2]*, Paul Byrne[2], Laurent Serres[2], Vaclav Sobolik[1]

[1]*LaSIE, University of La Rochelle, Pôle Sciences et Technologie, avenue Michel Crépeau, 17042, La Rochelle, France,*

[2]*LGCGM EA3913, Equipe Matériaux et Thermo-Rhéologie, Université Rennes 1, IUT de Rennes, 3 rue du Clos Courtel, BP 90422, 35704 Rennes Cedex 7, France*
*amina.meslem@univ-rennes1.fr, * Corresponding author*

## Abstract

Particle Image Velocimetry was used to investigate the flow field in an impinging lobed daisy hemispherical nozzle jet in comparison to its counterpart round jet, at a Reynolds number of 5620 based on the exit velocity and the equivalent diameter $D_e$ of the nozzle.

The limitations of the PIV technique in the vicinity of the target wall due to the laser scattering were addressed by using the electrodiffusion (ED) technique to determine the wall shear rate distribution. The distribution of the mass transfer coefficient is also obtained using the ED technique. The target wall is placed at a distance $H = 2D_e$ from the plane tangent to the nozzle, at the center of the orifice. The entrainment of ambient fluid in the free jet region, which is larger in the lobed jet compared to the round jet, feeds in turn the wall jet region.

The maximum wall shear rate was found significantly higher in the daisy jet, with an excess of 93% compared to the reference round jet. The maximum mass transfer is 35% higher in the former compared to the latter. Therefore, the hemispherical daisy nozzle is an excellent candidate in passive strategies to enhance local skin-friction and the subsequent local mass transfer at a constant exit Reynolds number.

***Keywords***—Electrodiffusion, PIV, lobed impinging jet, wall shear rate, mass transfer

## 1. Introduction

In turbulent jet, the global flow characteristics and the vortices which are forming in the jet near field are known to be dependent on the inlet conditions [1, 2]. The inlet conditions could be modified by active [3, 4], or passive control techniques [5, 6], which are commonly used to improve jet self-induction and mixing processes.

In the particular case of impinging jets which are used in many applications (metal and glass tempering, turbines blades and electronic components cooling, paper drying etc.), Gardon and Akfirat [7] showed that some seemingly anomalous heat-transfer phenomena at the target wall can be explained as effects of the turbulence occurring in jets. Turbulence is generated by the jet itself and by possible external disturbances and varies significantly with the nozzle shape, the upstream conditions and the position within the jet. Popiel and Boguslawski [8] confirmed that the configuration of the nozzle exit is the most important factor affecting the heat and mass transfer which occur in the neighborhood of the stagnation point. In spite of these first very significant observations, there are only a few studies dedicated to heat and mass transfer enhancement using jet passive control. Gao et al. [9] were the first authors to introduce passive control of an impinging jet for heat transfer enhancement. The authors found that the addition of triangular tabs at the pipe exit leads to a heat transfer enhancement with an excess of 25%. Lee et al. [10] showed that the peak of Nusselt number (*Nu*) generated by an impinging turbulent elliptic jet with an aspect ratio of 2.14, and having an exit Reynolds numbers *Re* of 5000, 10000 and 20000, is larger than that for its counterpart impinging circular jet. The authors speculated that this is due to the large entrainment rate and the large scale coherent structures which characterize elliptic jet. For a nozzle-to-plate distance $H = 2D_e$ ($D_e$ is the equivalent diameter based on the free area of the nozzle) and for $Re = 10000$ or 20000, the Nusselt number of elliptic jet exhibited, beyond the main maxima, a second peak.

Two peaks are also present on the radial distributions of local Nusselt number (*Nu*) or local Sherwood number (*Sh*), produced by circular impinging jets when the Reynolds number is high and the nozzle-to-wall distance is low. The first peak corresponds to the maximum of heat and mass transfer rate and occurs approximately at the nozzle radius. In some investigations [11-15], the location of the first peak is observed from $r = 0.5d$ *to* $r = 0.7d$ for $H < 4d$, where $d$ is the round nozzle diameter. This peak is attributed to the high turbulence intensity at the nozzle edge and to the direct impingement of large toroïdal Kelvin-Helmholtz (K–H) vortices originated in the mixing region [11]. The secondary peak occurs at the radial distance from the stagnation point ranging from $1.2d$ to $2.5d$ [11-16]. Katti et al. [17] found for a Reynolds

number in the range 4000-12000 an inflection point rather than a secondary peak in *Nu* radial distribution of the round jet for a nozzle-to-wall distance $H/d \leq 4$.

The secondary peak is either attributed to the transition from laminar to turbulent boundary layer in the wall jet region [11, 18] or to the unsteady separation of the counter-rotating secondary vortices that form near the wall bellow primary K–H vortices [19, 20]. Carlomagno and Andrea [21] give in their recent review of impinging jets a comprehensive description of secondary vortex dynamics.

With increasing Reynolds number, the location of the secondary peak moves outwards from the stagnation point and their imprint on heat and mass transfer increases [12].

Intuitively, one can assume a correlation between *Nu* or *Sh* and the skin friction. Hadziabdic and Hanjalic [19] observed a striking similarity between the instantaneous Nusselt number and the skin-friction coefficient a little further from the stagnation point. Also, the connection of the heat/mass transfer phenomena with the large-scale structures which develop in the free jet region or with the subsequent flow dynamics in the stagnation and wall jet regions is now recognized [13, 19, 22, 23]. Therefore, the control of large-scale structures in impinging jets is a key element in the strategy of heat and mass transfer optimization and control. The passive control based on nozzle geometry modifications is particularly attractive because of easy implementation in industrial applications.

Whereas numerous papers were published on the Nusselt number distribution generated by impinging jets, only a few studies have been dedicated to the analysis of the corresponding wall shear rate and Sherwood number distributions [11, 24-26]. Mass transfer and wall shear rate were deduced from the velocity field close to the impinging wall, and such a field is usually subjected to great uncertainties [26]. To a few exceptions belongs the study of Kataoka et al. [24] who measured local mass transfer and wall shear rate using the electrodiffusion (ED) method and pressure fluctuations using a piezoelectric transducer. However they used different electrodes for mass transfer (circular electrodes) and for wall shear rate (rectangular electrodes) measurements. Hence these two phenomena were not measured at the same place. In the recent works of Kristiawan et al. [27] and Meslem et al. [28] the ED technique was used to measure the wall shear rate in impinging cross-shaped jets and round jets, respectively. The mass transfer distributions on the target were not measured by the authors. They calculated mass transfer rate in the impingement region from the measured wall shear rate in the vicinity of the stagnation point under the assumption of uniform thickness of hydrodynamic and concentration boundary layer.

In the present study electrodes with a diameter of 0.5 mm were used alternately for the

measurement of wall shear rate and local mass transfer at the same place. Velocity fields were captured using Particle Image Velocimetry (PIV). Both experimental techniques (ED and PIV) are complementary as the PIV fails at the vicinity of the wall due to the laser scattering by the solid surface.

With these techniques, we examine the effects of nozzle exit configurations on the flow characteristics and on the resulting shear stress and mass transfer at the target wall. The geometry of the impinging jets considered in the present study are different from the previous. They are daisy and round jets generated by innovative hemispherical nozzles devoted to a personalized ventilation headset [29]. The daisy nozzle is a six-lobe orifice perforated on a hemispherical surface (DO/H). The round nozzle is a circular orifice, having the same free area as DO/H, perforated on a same hemispherical surface. The study is conducted at constant free area of the nozzle and constant volumetric flow rate. This specific choice is related to the aimed application of personalized ventilation headsets [29]. For others applications where the energy conservation is required, further investigations should be conducted at the same power input.

## 2. Theory

The electrodiffusion (ED) method is based on the measurement of the limiting diffusion current on a working electrode (probe). For the total current $I$ through a circular electrode in a viscosimetric steady flow with parallel streamlines and uniform wall shear rate $\gamma$, the formula corresponding to Leveque's equivalent formula for heat transfer was established by Reiss and Hanratty [30]:

$$I = \frac{0.884\pi}{3^{1/3}\Gamma(4/3)} nFc\gamma^{1/3}D^{2/3}R^{5/3} \qquad (1)$$

where $\Gamma$ is the gamma function, $n$ is the number of electrons involved in the electrochemical reaction ($n = 1$ for the potassium ferro- and ferricyanide system), $F$ is the Faraday constant, $c$ is the bulk concentration of the active ions, $D$ is the diffusivity of the active ions, and $R$ is the radius of the electrode.

In the case of an impinging circular jet, the streamlines in the wall vicinity spread radially from the stagnation point. There is effect of the velocity component normal to the wall, which attenuates with increasing radial distance $r$ from the stagnation point. Kristiawan et al. [27]

arrived at the conclusion that the error using Eq.1 for calculation of $\gamma$ makes only 2.1 % at a dimensionless radial distance *r/R* equal to 4.

The limiting diffusion current is controlled by the transfer of active species to the working electrode. Under the assumption that the transfer resistance on the auxiliary electrode is negligible in comparison with that on the working electrode, the coefficient of mass transfer can be calculated using the following relation:

$$k = \frac{I}{S_{el}\, F\, c} \tag{2}$$

where $S_{el}$ is the active surface of the working electrode. The Sherwood number *Sh* is then defined by:

$$Sh = \frac{k\, D_e}{D} \tag{3}$$

where $D_e$ is the nozzle diameter and *D* the diffusion coefficient of active species.

## 3. Experimental setup

### 3.1. Jet flow generation and electrodiffusion measurements

Detailed description of the experimental device can be found in the paper by Kristiawan et al. [27], El Hassan et al [22] or Meslem et al. [28]. It consists of a Plexiglass reservoir, a gear pump, a nozzle and a target with electrodes (Figure 1 (a)).

The target (Figure 1 (b)), was manufactured of a Plexiglas disc with a diameter of 100 mm and thickness 17 mm by first drilling the holes to insert the electrodes. The electrodes were fabricated of a 0.5 mm platinum wire which was coated electrophoretically with a deposit of a polymeric paint. The electrodes were glued with an epoxy resin into the Plexiglas disc, so that the tops of the platinum wires just projected above the platinum disc. Nickel sheets with an area of 0.15 $m^2$ and the stainless steel tube were used as the auxiliary electrode (anode). The area of the nickel sheets and the stainless steel tube was 80 times superior to the platinum disc area. To measure only the phenomena that happen on the measuring electrode (cathode), the area of the auxiliary electrode (anode) should be large enough. Measured currents in our experiments did not change if the anode area was enlarged which was the proof of the sufficiency of the anode area.

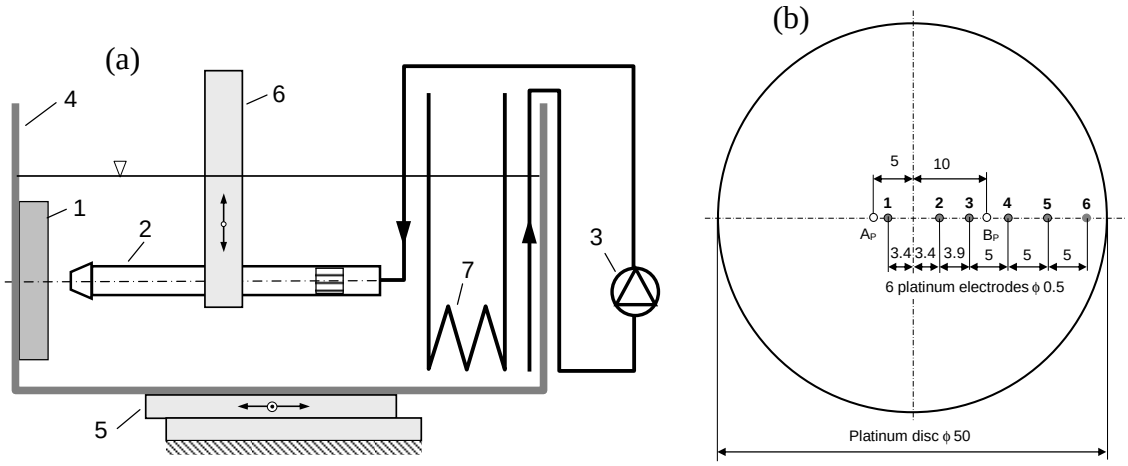


Figure 1: (a) Diagram of apparatus,1 target disc with electrodes, 2 tube with nozzle and honeycomb, 3 pump, 4 reservoir, 5 compound table, 6 nozzle holder, 7 cooling coil; (b)Target disc with electrodes row, 1-6 electrodes $\phi$ 0.5mm, $A_P$ and $B_P$ are the limits of stagnation point displacement

The reservoir with the fixed target was placed on a sliding compound table which permitted horizontal displacement of the target relative to the nozzle. The wall shear rate and local mass transfer were measured at 29 positions separated by 0.5 mm. The first position of the stagnation point (see Figure 1 (b)) was in the point $A_P$ (6.2 mm left from the disc centre), and the last position in the point $B_P$ (10.8 mm right from the disc centre).

The test fluid was a 5 mol/m$^3$ equimolar potassium ferri/ferrocyanide aqueous solution with 1.5% mass $K_2SO_4$ as the supporting electrolyte. The solution had a density $\rho$ = 1006 kg/m$^3$, kinematic viscosity $\nu$ = $1.06 \cdot 10^{-6}$ m$^2$/s and diffusivity $D$ = $7.5 \cdot 10^{-10}$ m$^2$/s at 20°C. The resulting Schmidt number was 1410.

As aforementioned, in this study a daisy hemispherical nozzle jet was compared to a reference round hemispherical nozzle jet. Schematics of the nozzles are shown in Figure 2. They are given by the projection of a plane daisy orifice or a plane round orifice onto a spherical surface (Daisy Orifice made on a Hemisphere, DO/H in Figure 2 (b) and Round Orifice made on a Hemisphere, RO/H in Figure 2 (a)). The two nozzles had a same equivalent diameter $D_e$ = 7.8 mm, corresponding to the projection on the plane of the curved orifice. The Reynolds number based on $D_e$ and the jet bulk-velocity ($W_b = 4Q_0/\pi D_e^2$) is $Re_b$ = 5620. The distance $H$ between the plane tangent to the nozzle at the center of the orifice and the target wall is kept constant ($H = 2D_e$) for all the measurements.

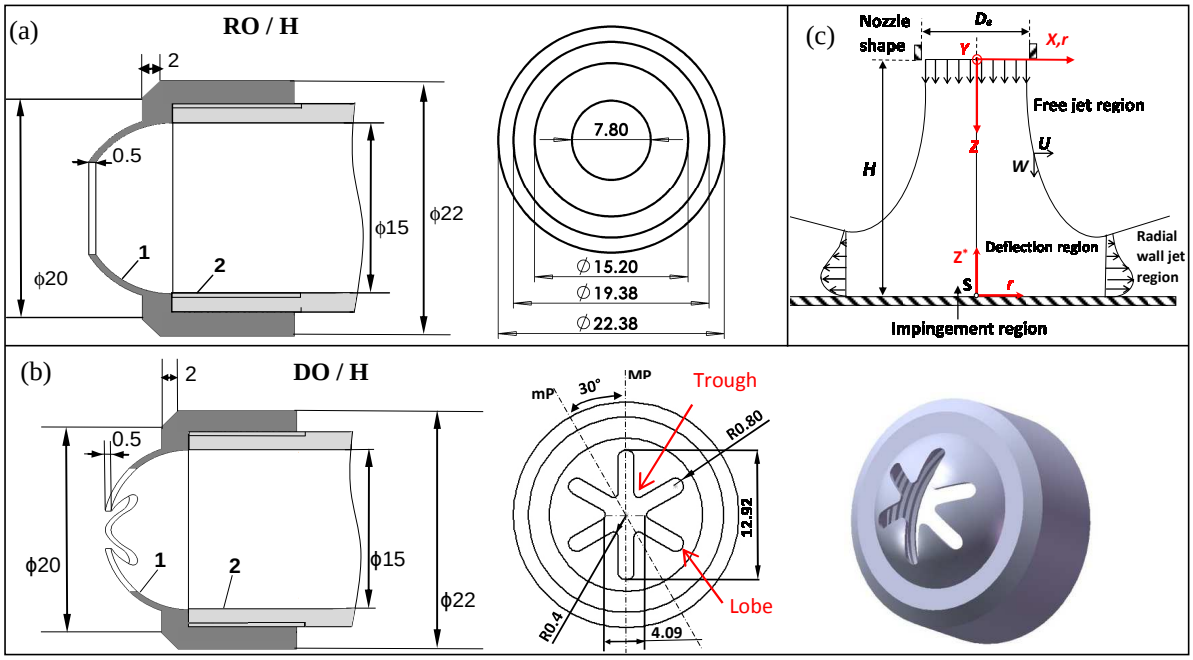


Figure 2: Sketch of nozzle geometry: (a) Round-Orifice on Hemisphere (RO/H); (b) Daisy-Orifice on Hemisphere (DO/H), 1 – Hemispherical surface supporting the orifice, 2 – Tube; (c) Schematic description of impinging jet on a flat plate and associated system coordinates

### 3.2. Velocity field measurements

The flow field was investigated by a 2D2C PIV (two velocity components in-plane). The experiments were carried out with a Quantel BigSky 200 mJ double-pulsed Nd:Yag laser and a FlowSense EO (CCD) camera of 2048×2048 pixels resolution with a pixel size of 7.4×7.4 μm$^2$. The total field of view is about $2D_e$×$6D_e$ to cover free and wall jet regions (Figure 2 (c)). The light sheet optics produces a laser sheet of less than 1 mm in thickness. The maximum acquisition frequency of the PIV system is 15 Hz. The seeding particles are glass hollow spheres of 9 to 13 μm in diameter and 1.1g/cm$^3$ in density.

For each experiment, 500 couples of images were acquired and post-processed using DynamicStudio Dantec software. The velocity distribution in the total field of view ($2D_e$×$6D_e$) was calculated using an adaptive multi-grid correlation algorithm [31] handling the window distortion and the sub-pixel window displacement (128×128, 64×64, and 32×32 pixels) and 50% overlapping. The prediction-correction validation method of multi-grid algorithm identified on average less than 1% erroneous velocity vectors, which are replaced using a bilinear interpolation scheme. For all the experiments, the uncertainty of the measurement due to displacement error was estimated using the theoretical analysis of

Westerweel [32]. When adding the global bias errors, the total uncertainty is estimated to be in the range of 2 to 3.5% outside the boundary layer. The uncertainty rises near the impinging plate due to laser scattering, so that the boundary layer is not accessible using PIV technique. This difficulty is bypassed using another measurement technique, which is the electrodiffusion (ED) method described above.

## 4. Results and discussion

### 4.1. Flow characteristics

In this section the global features of the daisy impinging jet is examined in comparison to the reference round jet. The analysis focuses on both free and wall jet regions defined in the Figure 2 (c). We grouped in Table 1 the characteristics of each jet.

As will be shown later on, in the daisy jet, the centerline velocity is almost constant in the region $0<Z<1D_e$. However, the centerline velocity in the round orifice jet increases in the region $0<Z<0.5D_e$. That is the reason why, the inlet velocity $W_0$ is defined in the present study on the plateau of each jet, i.e. at $Z = 0.5D_e$ (Table 1). The ratio $W_0 / W_b$, where $W_b = 0.77$ m/s is the bulk velocity defined by the ratio of the initial volumetric flow rate $Q_0$ on the free area of the nozzle, highlights the level of the flow acceleration, which is somewhat higher in the daisy jet than in the round jet. The momentum thickness $\theta_0$, the displacement thickness $\delta^*_0$ in their non-dimensional form, and the shape factors $H^*$ are given in Table 1.

Table 1: Initial experimental conditions

| Nozzle | Symbol | $W_0 = W(Z = 0.5D_e)$ (m / s) | $W_0/W_b$ | $\delta^*_0/D_e$ | $\theta_0/D_e$ | $H^* = \delta^*_0/\theta_0$ |
|---|---|---|---|---|---|---|
| Daisy Orifice on Hemisphere - Major Plane | DO/H - MP | 1.13 | 1.47 | 0.061 | 0.02 | 3.01 |
| Daisy Orifice on Hemisphere - minor Plane | DO/H - mP | 1.13 | 1.47 | 0.051 | 0.018 | 2.91 |
| Round Orifice on Hemisphere | RO/H | 1.07 | 1.39 | 0.041 | 0.015 | 2.68 |

In Figure 3, spatial developments of the daisy jet (Figure 3 (a1) and (a2)) in their respective major plane (MP) and minor plane (mP) were compared to the reference round orifice jet (Figure 3 (b)). MP and mP refer to planes cutting the nozzle in the directions of a lobe and a trough respectively (see Figure 2 (b)). In-plane mean velocity profiles, using the representation of ($W$, $U_r$) vectors, are plotted in the free jet region and are superimposed to radial velocity $U_r$ isocontours for absolute values larger or equal to 0.1m/s (i.e. 14% of $W_b$). This way, the regions with large radial velocity are evidenced in the observed planes. As expected, in the wall jet region, the flow spreads in radial directions parallel to the wall, resulting in high values of $U_r$, although the corresponding contours are different in shape for the two jets and are also different in shape between the MP and mP of the daisy jet. In the free jet region, the radial velocity $U_r$ is lower than 0.1m/s, except in the MP of the daisy jet (Figure 3 (a2)) where one observes an outwards movement at the jet periphery. In this plane, velocity profiles at the jet exit are two-step shaped due to the presence of two shear layers: the inner shear layer between the jet central core and the lobes, and the outer shear layer between the jet flow and its ambience. The outwards radial velocity $U_r$ is high in the outer shear layer of the MP because of the curvature of the lobes on the hemispherical surface supporting the daisy orifice. The subsequent outward high radial velocities lead to the conservation of the two-step distribution in the MP, until the stagnation point.

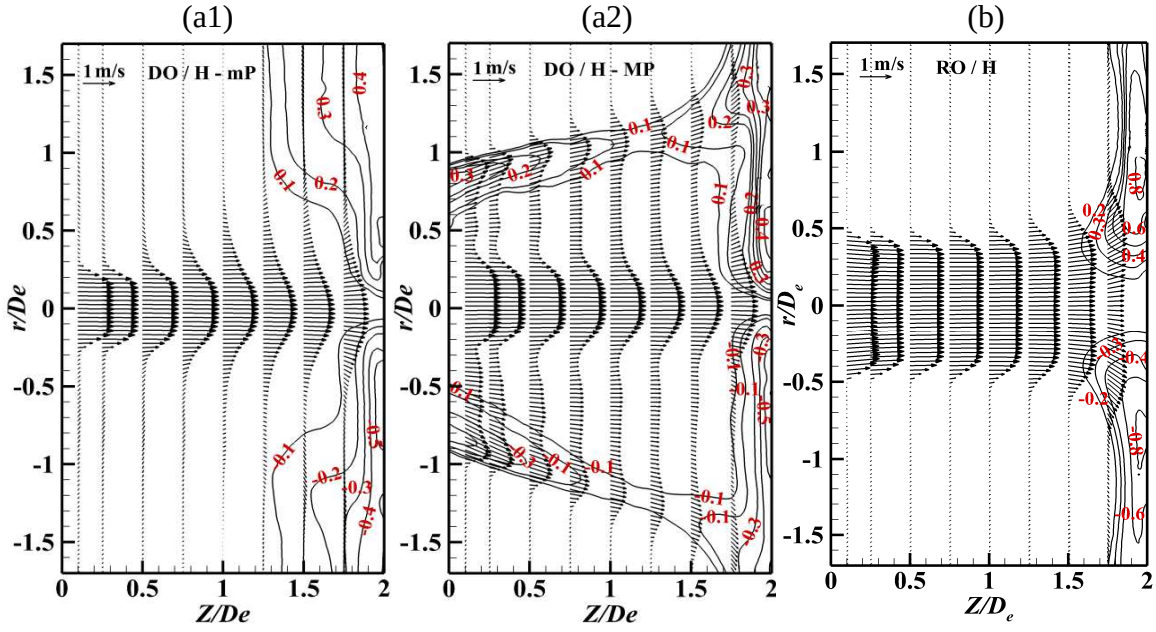


Figure 3: In-plane velocity vectors ($W$, $U_r$) in the free jet region and radial velocity contours: (a) daisy orifice on hemisphere (DO/H) – minor plane (a1) and major plane (a2); (b) round orifice on hemisphere (RO/H)

Another interesting feature of the daisy jet is the large spreading of its radial wall flow in the minor plane mP, compared to counterpart radial flows in the MP of the same jet and the longitudinal plane of the reference round jet. Note that the jet from the lobed hemispherical nozzle is characterized by a large entrainment of ambient fluid. It was shown in our previous investigation of a free jet from a lobed hemispherical nozzle [33] that entrainment of surrounding fluid occurs into the lobe troughs whereas the jet fluid is ejected in the top of the lobes (see Figure 2 (b) for troughs and lobes definitions). This particular dynamics was explained by streamwise secondary vortices organization which are produced by the double shear effect of the lobed lip of the orifice and the curved surface supporting the lobed orifice. In impinging jet configuration, the target wall confines the free stream region and the entrained fluid in the mP of the lobed jet feeds the wall jet region in the same plane. The large expansion of the radial wall jet region observed in the mP (Figure 3 (a1)) of the lobed jet is the results of the previously presented dynamic phenomena.

To access quantitative flow characteristics, the streamwise mean velocity $W_C$ at the jet centerline and the jet thickness $r_{0.1}$ in the free jet region are plotted in Figure 4 (a) and (d), respectively. The jet thickness $r_{0.1}$ is the radial distance from the centerline to the point where the streamwise mean velocity reached $W = 0.1W_C$.

In Figure 4 (a), the subfigure compares the round jet data of the present study to those of Baydar and Ozmen [34] obtained with a round pipe impinging jet at a high Reynolds number of $3\times10^4$. To our knowledge, the hemispherical round nozzle of this study has never been used for impinging jet generation, so there were no available literature data regarding the flow characteristics and the corresponding transfer processes. However, and despite the differences in nozzles geometry, close agreement between the two curves beyond the *vena contracta* region is observed.

As evidenced in Figure 4 (a), the axial velocity $W_C$ achieves zero at the stagnation point S of each jet. However, before impingement, axial velocity is significantly higher in the daisy jet compared to the reference round jet. A difference between the two jets is also visible near the jet exit. Whereas in the lobed jet axial velocity is almost constant from the exit till $Z = 1D_e$, in the round jet axial velocity increases between $Z= 0$ and $Z = 0.5D_e$ due to the vena contracta effect. The absence of axial velocity increase at the exit of the lobed jet (Figure 4 (a)) may be due to the high entrainment which characterizes this jet [33]. The streamwise velocity profiles at $Z = 1D_e$ and $Z = 1.9D_e$ are shown on Figure 4 (b) and (c). The profile of the reference round jet is still flat until near the impingement plate (Figure 4 (c)) while for the lobed jet, as the jet evolves, the axial

momentum diffuses radially and the imprint of the nozzle shape in the major plane disappears progressively.

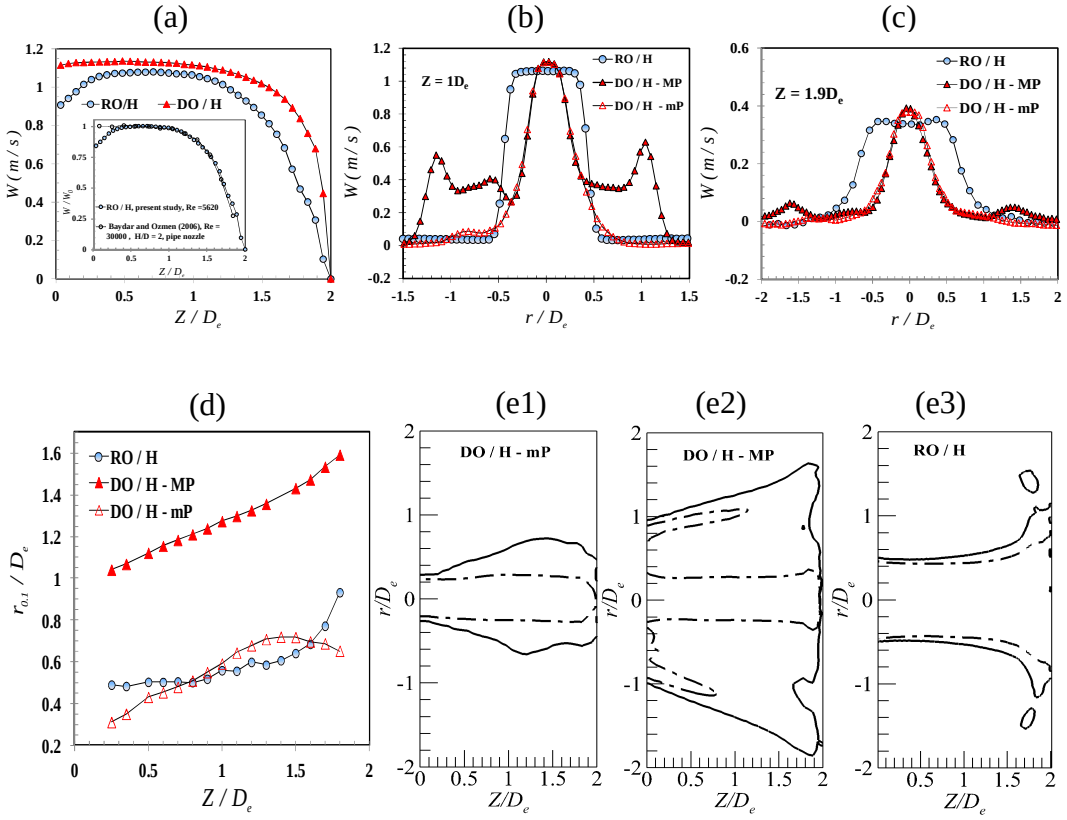


Figure 4: Changes of mean axial velocity along the jet centerline – the hemispherical round orifice nozzle jet is compared to the literature pipe jet [34] (a); Streamwise velocity profile at $Z$=1$D_e$ (b), and $Z$=1.9$D_e$ (c); Jet widths $r_{0.1}$ in the free jet region (d); Isocontours $W/W_C$ = 0.5 (dashed line) and $W/W_C$ = 0.1 (solid line): (e1) daisy orifice on hemisphere-minor plane, (e2) daisy orifice on hemisphere-Major plane, (e3) round orifice on hemisphere

Flow spreading in the free jet region is quantified by the measure of the jet widths $r_{0.1}$ (Figure 4 (d)). The jet width $r_{0.1}$ in the daisy jet increases in both mP and MP. However in the mP, $r_{0.1}$ decreases somewhat near the impinging plate. Flow contraction in the mP is confirmed by the shape of the Isocontours $W/W_C$ = 0.5 and $W/W_C$ = 0.1 shown in Figure 4 (e1)). This could be explained by the confinement of the free jet region, under the effect of the large expanded wall jet region in this plane (Figure 3 (a1)). As evidenced by Figure 4 (e2) and (e3), no contraction is present neither in the MP of DO/H nor in the longitudinal plane of RO/H.

To analyse the flow in the wall jet region, mean radial velocity $U$ profile at $r$ = 2.5$D_e$ and maximum radial velocity $U_{max}$ were plotted (Figure 5). In order to make a comparison with the theoretical solution of Glauert (Figure 5 (a)), the mean radial velocity $U$ was normalized

with the corresponding maximum radial velocity $U_{max}$, and plotted against $Z^*/Z^*_{0.5}$ (the $Z^*$ axis takes its origin on the target wall, $Z^* = H - Z$ and $Z^*_{0.5}$ is the Z* position in the wall jet where the radial velocity $U$ takes the value $0.5U_{max}$, see Figure 2). The profile of our round jet matched with the Glauert [35] solution. The profiles in the mP and MP of the lobed jet were slightly different from the reference profile and Glauert theoretical solution in the wall vicinity and in free jet region. Recall that in the vicinity of the wall, the PIV measurements are questionable due to laser scattering by the wall surface.

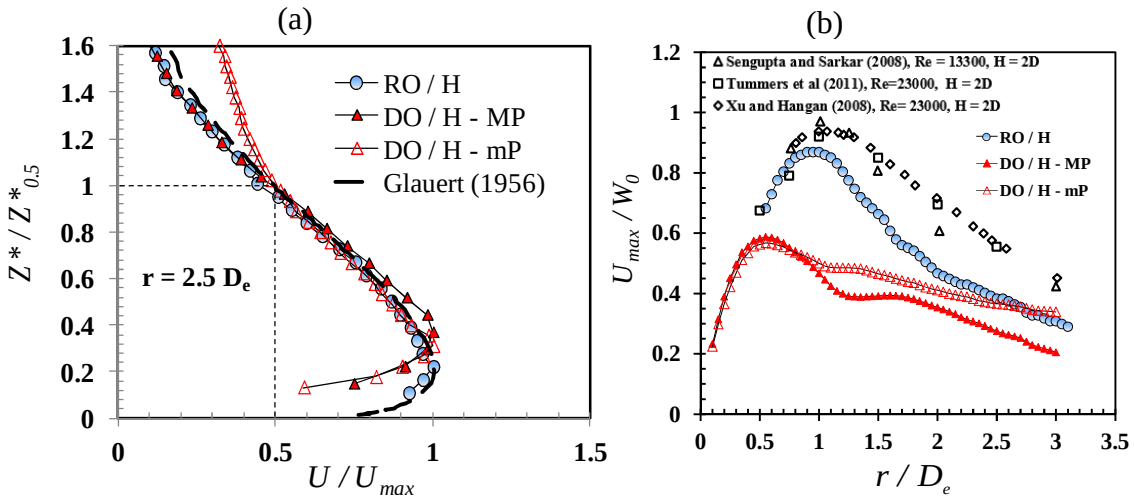


Figure 5: (a) Normalized radial mean velocity distributions at $r = 2.5D_e$ - Comparison to the predicted curve of Glauert [35] with $\alpha = 1.3$. (b) Normalized maximum radial mean velocity distributions, comparison to the literature – the round nozzle in [36, 37] is a pipe and in [38] a convergent connected to a short pipe

Although the uncertainties on velocity measurements could be high near the target wall, we decided to examine the radial changes of the maximum velocity in the radial wall jet region. Figure 5 (b) shows the variation of the normalized maximum velocity $U_{max}/W_0$ of the velocity profile in the radial wall jet region as a function of the normalized radial distance from the stagnation point. Two regions can be identified: the first is where the radial velocity $U_{max}$ increased and it ends where $U_{max}$ reached its highest value around the location $r = 1D_e$ for RO/H nozzle jet, and $r = 0.55D_e$ for DO/H nozzle jet (Figure 5 (b)). This value was almost equal to the jet exit velocity $W_0$ in the round reference jet. This is consistent with the results of Tummers et al. [36] and Xu and Hangan [37].

The ratio of the location of the highest value of $U_{max}$ to the radial location of the inflection point of mean streamwise velocity profile just before impingement (the profile at $Z = 1.9D_e$

was considered, see Figure 4 (c)) is constant and approximately equal to 1.7 for the two jets. The considered inflection point of streamwise velocity profile corresponds to the location of vortices in the mixing region, which then striking the target wall. In the second region, maximum velocity decreased. The DO/H nozzle jet was significantly different from the reference round jet in terms of radial maximum velocity distribution. The magnitude of $U_{max}/W_0$ was about 32% lower than in the RO/H nozzle jet. In the major plane two small peaks were present as an imprint of the two-step velocity distribution in the free jet region.

### 4.2. Wall shear rates distributions

Local and instantaneous wall shear rate γ was acquired using the electrodiffusion method (ED) described above. During the wall shear rate measurements the platinum wires worked as the cathode and the platinum disc (Figure 1 (b)) with the nickel sheets as the anode.

To measure γ values, the signals were recorded with a sampling frequency of 500 Hz during a period of 40 sec. To well capture the details of γ profiles, the stagnation point S has been moved horizontally 29 times in the range limited by the points $A_P$ and $B_P$ on the target (Figure 1 (b)) with a step of 0.5mm. Thereby, several values of the wall shear rate measured by different electrodes at similar radial distances $r$ from the stagnation point $r = 0$, were obtained. Based on the comparison of the measured values for a given radial position, it was observed that the repeatability is insured with a maximum deviation of ±5% of the mean value.

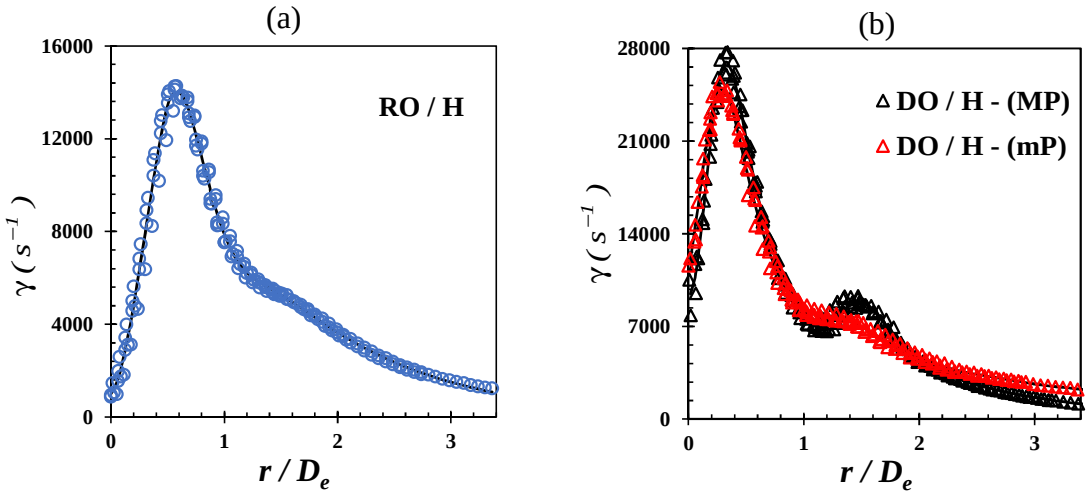


Figure 6: Radial profiles of mean wall-shear rate: (a) round jet; (b) daisy jet - major plane (MP) and minor plane (mP)

The maximum value $\gamma_{max}$ of wall shear rate is equal to 14000 $s^{-1}$, 27000 $s^{-1}$ and 25000 $s^{-1}$ for the RO/H, DO/H-MP and DO/H-mP, respectively (Figure 6). Hence, the local wall shear rate is nozzle geometry dependent, and is significantly higher in DO/H nozzle jet than in the reference round jet RO/H with an excess of 93%. Hence, the DO/H nozzle jet is an excellent candidate in passive strategies to enhance skin friction without changing the volumetric flow rate.

In each jet, the wall shear rate increases monotonically with the radial distance, reaches its maximum $\gamma_{max}$, and then decreases. In the RO/H, $\gamma_{max}$ appears at $r/D_e$ = 0.58, which falls in the range of $0.6D_e$ - $0.7D_e$ reported in the literature [24, 26] for the round impinging jet with nozzle-to-wall distance $H < 4D_e$. As for the daisy jet, the maximum is located at $r/D_e$ = 0.33 and $r/D_e$ = 0.30 in the MP and mP, respectively. The presence of a secondary peak around $r/D_e$ = 1.5 in the major plane MP of DO/H nozzle jet can be noticed.

It is reported in the literature that the first peak in $\gamma$ distribution is related to the impingement of the K-H vortices on the wall [11, 12], whereas the secondary peak, pertinent only for small nozzle-wall distances and high initial Reynolds numbers, is due to secondary counter-rotating vortices and to the associated turbulence produced [19, 22], or to a transition from a laminar to a turbulent boundary layer [14, 16]. According to the literature, the first peak in $\gamma$ distribution of the DO/H or RO/H nozzle jet is the imprint on the wall of the K-H vortices which develop in the outer shear layer between the jet flow and its ambience. Nonetheless the second peak in the MP of DO/H nozzle jet corresponds to the imprint on the wall of the inner shear layer present in this plane (Figure 3 (a2)) between the jet central core and its lobes. No secondary peak is visible in the RO/H jet (Figure 6 (a)) because the Reynolds number is moderate.

### 4.3. Mass transfer distributions

During the mass transfer measurements the platinum wires and the platinum disc worked as cathode and the nickel sheets as anode. In this case, the platinum disc was maintained at the same potential as the worked electrodes. Whereas the platinum disc was used to measure the global mass transfer, the platinum wires were used to measure the local mass transfer.

As it was the case in the wall shear rates measurements, the radial distributions of the local mass transfer were obtained by moving the stagnation point S horizontally in the range limited by the points $A_P$ and $B_P$ on the target (Figure 1 (b)). Figure 7 shows the obtained distribution of the local Sherwood number *Sh* along the radial axis, *r*, for the two considered jets. Similarly to what we observed for the wall shear rate $\gamma$, the maximum value of the local

*Sh* is nozzle geometry dependent and is equal to 1220 and 1650 for the RO/H and DO/H, respectively. The local Sherwood number is then 35% higher for DO/H compared to RO/H. Given the fact that the maximum value of *Sh* corresponds to the maximum mass transfer, the present results demonstrate that the use of a lobed nozzle not only improves wall shear rate, but also increases local mass transfer, which let to assume that the latter is correlated to the former.

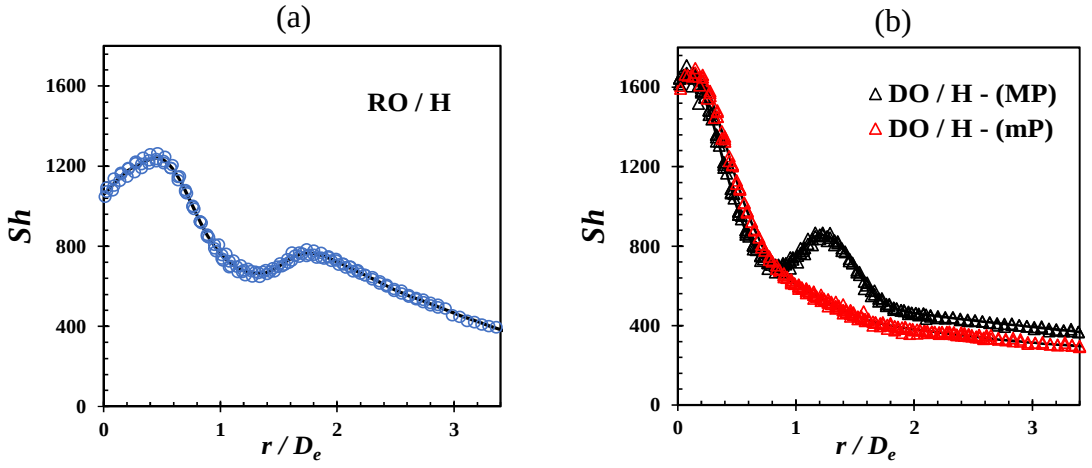


Figure 7: Radial distribution of the Sherwood number: (a) round jet; (b) daisy jet - major plane MP and minor plane mP

The maximum of *Sh* occurs at $r = 0.55D_e$ and $0.15D_e$ for the RO/H and DO/H, respectively (Figure 7). Hence, the first peak of *Sh* is shifted from the stagnation point, as it was also observed by Kataoka et al. [24] in the core jet region of a convergent impinging jet. The authors explained that the mass transfer is very sensitive to the velocity turbulence which is still low on the jet axis in the potential core region and increases near the nozzle edge. In Vallis et al. investigation [39] the peak of *Sh* for nozzle to plate distance in the range 5 to 20 nozzle diameters appears on the stagnation point; it is expected here that the core jet region is already consumed at 5 nozzle diameters, a position from which the turbulence rises on the jet axis. The fact that the maximum of *Sh* in DO/H is closer to the jet axis compared to the RO/H is not surprising. In fact, the jet core region is shorter in the former than in the later due to its higher self-induction [33].

Another comparison with the available literature data is given in figure 8 (a) for the reference round jet. When taken into account the Schmidt number *Sc* and the Reynolds number *Re*, our result agrees very well in shape and maximum level value with the data of Angioletti et al. [40]. The first and the second peaks appear at the same location even if that of Angioletti et al. is very weak due to their low Reynolds number (*Re* = 1000).

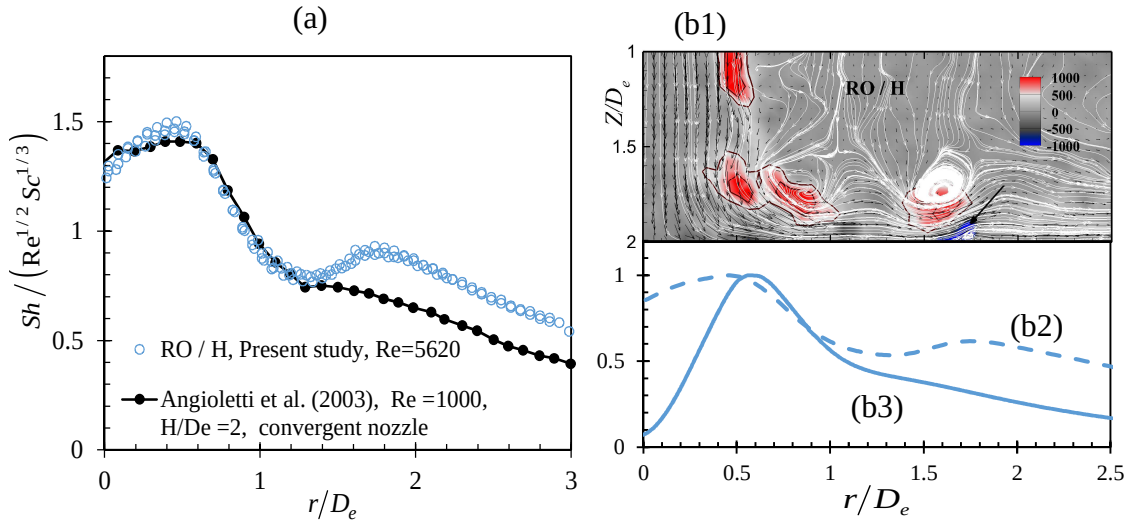


Figure 8: (a) Comparison of local Sherwood number of the circular nozzle jet with literature data [40]; (b1) Instantaneous vorticity field $\omega_Y = \left(\frac{\partial U}{\partial Z} - \frac{\partial W}{\partial X}\right)\frac{D}{W_0}$ - arrows indicate secondary vortices on the target; (b2) $Sh/Sh_{\max}$, (b3) $\gamma/\gamma_{\max}$

In numerous studies of heat transfer, as in Lee and Lee [41] and Colucci and Viskanta [42] investigations, the same behavior was observed for the Nusselt number (*Nu*) distribution: the maximum of *Nu* in the core jet region is shifted from the stagnation point, whereas in the jet transition region and downstream the maximum of *Nu* appears at the stagnation point.

The secondary peak in *Sh* distribution is at $r = 1.8D_e$ in RO/H nozzle jet and at $r = 1.3D_e$ in the major plane MP of the DO/H nozzle jet (Figure 7).

As it was emphasized for the wall shear rate, the second peak in *Sh* distribution in the MP of DO/H nozzle jet corresponds to the imprint on the wall of the inner shear layer present in this plane (Figure 3 (a2), Figure 4 (b) and 4 (c)) between the jet central core and its lobes.

In the case of the reference round jet, the origin of the secondary peak in *Sh* distribution could be related, as for *Nu* distribution, to the reattachment of a recirculation bubble [19-21].

As evidenced in Figure 8 (b), the first peak in *Sh* distributions appears in the region where the K-H vortices strike the target and its secondary peak emerges at the position where appear counter-rotating vortices on instantaneous vorticity field; the secondary vortices are designated by an arrow in Figure 8 (b1). If we advance the similarity between the secondary peak of *Sh* and the secondary peak of *Nu*, the observation made above is consistent with that of Hadziabdic and Hanjalic [19]. From their LES simulation of a round impinging jet, the authors observed that the secondary peak in *Nu*, (pertinent only for small $H/D_e$ and high

Reynolds numbers) is caused by the reattachment of the recirculation bubble and by the associated turbulence production, as well as the subsequent strong advection. The conclusions of Hadziabdic and Hanjalic [19] are consistent with those of Carlomagno and Andrea [21], which give in their recent review a comprehensive description of secondary vortex dynamics in impinging jets.

The absence of a secondary peak in *Sh* distribution in the minor plane mP of the DO/H nozzle jet could be explained by the fact that K-H vortices in this jet are very small. In fact, the near field of lobed jet is dominated by secondary vortices generated by the undulated nozzle lip [43, 44], whereas the near field of circular jet is dominated by toroidal K-H vortices [43-46].

For the two nozzles RO/H and DO/H, the global Sherwood number is obtained from the measured limiting diffusion current through the platinum disc of $3.2D_e$ in radius (Figure 1 (b)) centered on the stagnation point S. The values obtained are 618 and 520 for the RO/H and DO/H nozzle jet, respectively, thus leading to the relative difference of 19%. In the specific conditions of the present study (Reynolds number, nozzle to plate distance and the area of the platinum disc), the present result shows that despite the high performance of DO/H nozzle jet in local mass transfer, its global mass transfer is lower than the reference round jet. The DO/H nozzle jet is globally more expanded than the reference RO/H nozzle jet (Figure 3). Hence, measurements of the global mass transfer on a larger platinum disc should be performed to definitively conclude on the higher global mass transfer performance of the DO/H nozzle jet relatively to the RO/H nozzle jet.

Assuming the axial symmetry of the RO/H nozzle jet, its global Sherwood number $Sh_g$ can be obtained from the integration of the fitted curve of the local Sherwood number distribution as follows:

$$Sh_g(r) = \frac{2}{r^2}\int_0^r Sh(\rho)\times\rho\, d\rho \qquad (4)$$

The fitted curve of *Sh* distribution (Figure 7 (a)) was obtained using a cubic spline interpolation. The integration value (648) over a disc ($r = 3.2D_e$) obtained using Eq. 4 is 5% higher than the measured value (618). The difference is rather low and provides confidence in the quality of our measurements.

## Conclusions

The present study confirmed the linkage between the wall shear stress and the mass transfer induced by the jet impinging the target orthogonally on the one hand, and the jet nozzle geometry on the other hand. Two nozzles with a same equivalent exit diameter $D_e$ were considered. A six-lobed daisy orifice perforated on a hemispherical surface was compared to a reference round orifice perforated on a same hemispherical surface. The nozzle-to-wall distance was equal to $2D_e$ and the wall is a platinum disc of $3.2D_e$ in radius. The study is conducted at a same volumetric flow rate for the two jets, leading to the same exit Reynolds number of 5620. This specific choice is related to the aimed application, i.e. the personalized ventilation headset. By combining the Particle Image Velocimetry (PIV) and the electrodiffusion (ED) technique, mean velocity fields along with wall shear rates and mass transfer were analyzed.

The daisy jet is characterized by a larger spreading rate in its major plane MP compared to the one in its minor plane mP, and to the longitudinal plane of the round jet. In the MP of the daisy jet, the velocity profiles are two-step shaped due to the presence of two shear layers: the inner shear layer between the jet central core and the lobes, and the outer shear layer between the jet flow and its ambience. The two-step distribution in the MP is present until the target. In the outer shear layer, the radial velocity is high and is oriented outwards because the imprint of the curvature of the hemispherical nozzle lobes on the flow.

As the entrainment of the ambient fluid mainly occurs in the troughs regions of the hemispherical daisy lobed orifice, the expansion of the radial wall jet region in the mP is significantly higher than in the MP of the same jet.

The maximum wall shear rate and the maximum local mass transfer coefficient were found significantly higher in the daisy jet, with an excess of 93% and 35% , respectively, compared to the reference round jet.

The global mass transfer on a target disc is 19% lower for the daisy jet compared to the reference round jet. As the daisy jet is globally more expanded than the reference round jet, measurements of the global mass transfer on a larger target disc should be performed to definitively conclude on the higher global mass transfer performance of the lobed jet relatively to the round jet. The global mass transfer of the round jet obtained by the integration of the local Sherwood number distribution, using an assumption of an axial symmetry of the flow, is 5% higher than the measured value. The difference is rather low and provides confidence in the quality of measurements.

**Acknowledgments**

This work was supported by the Grants of the French National Research Agency - Project FLUBAT – ANR-12-VBDU-0010

**References**

1. Husain, Z.D. and A.K.M.F. Hussain, *Axisymetric Mixing Layer: Influence of the Initial and Boundary Conditions.* AIAA Journal, 1979. **17**(1): p. 48-55.
2. Xu, G. and R.A. Antonia, *Effect of different initial conditions on a turbulent round free jet.* Experiments in Fluids, 2002. **33**: p. 677–683.
3. Hussain, A.K.M.F. and K.B.M.Q. Zaman, *The 'preferred mode' of the axisymetric jet.* Journal of Fluid Mechanics, 1981. **110**: p. 39-71.
4. Hussain, F. and H.S. Husain, *Elliptic jets. Part1. Characteristics of unexcited and excited jets.* Journal of Fluid Mechanics, 1989. **208**: p. 257-320.
5. Zaman, K.B.M.Q., M.F. Reeder, and M. Samimy, *Control of axisymmetric jet using vortex generators.* Physics of Fluids, 1994. **6**(2): p. 778-793.
6. Gutmark, E.J. and F.F. Grinstein, *Flow Control with Noncircular Jets.* Annual Reviews of Fluid Mechanics, 1999. **31**: p. 239-272.
7. Gardon, R. and J.C. Akfirat, *The role of turbulence in determining the heat-transfer characteristics of impinging jets.* International Journal of Heat and Mass Transfer, 1965. **8**: p. 1261-1272.
8. Popiel, C.O. and L. Boguslawski. *Effect of Flow Structure on the heat or mass transfer on a Flat plate in Impinging Round jet*. In *2nd UK National Conf. on Heat Transfer*. 1988.
9. Gao, N., H. Sun, and D. Ewing, *Heat transfer to impinging round jets with triangular tabs.* international Journal of Heat and Mass Transfer, 2003. **46**(14): p. 2557-2569.
10. Lee, S.-J., J.-H. Lee, and D.-H. Lee, *Local heat transfer measurements from an elliptic jet impinging on a flat plate using liquid crystal.* International Journal of Heat and Mass Transfer, 1994. **37**(6): p. 967–976.
11. Kataoka, K. and T. Mizushina. *Local enhancement of the rate of heat-transfer in an impinging round jet by free-stream turbulence*. In *Heat Transfer 1974; Proceedings of the Fifth International Conference, Tokyo, Volume 2*. 1974. Tokyo.
12. Lee, J. and S.J. Lee, *The effect of nozzle configuration on stagnation region heat transfer enhancement of axisymmetric jet impingement.* International Journal of Heat and Mass Transfer, 2000. **43**: p. 3497-3509.
13. Violato, D., et al., *Three-dimensional vortex dynamics and convective heat transfer in circular and chevron impinging jets.* International Journal of Heat and Fluid Flow, 2012. **37**: p. 22–36.
14. Roux, S., et al., *Experimental investigation of the flow and heat transfer of an impinging jet under acoustic excitation.* International Journal of Heat and Mass Transfer, 2011. **54**: p. 3277–3290.
15. Ozmen, Y. and E. Baydar, *Flow structure and heat transfer characteristics of an unconfined impinging air jet at high jet Reynolds numbers.* Heat and Mass Transfer, 2008. **44**(11): p. 1315-1322.
16. Lytle, D. and B.W. Webb, *Air jet impingement heat transfer at low nozzle-plate spacings.* International Journal of Heat and Mass Transfer, 1994. **37**(12): p. 1687-1697.

17. Katti, V., S.N. Yasaswy, and S.V. Prabhu, *Local heat transfer distribution between smooth flat surface and impinging air jet from a circular nozzle at low Reynolds numbers.* Heat and Mass Transfer, 2011. **47**(3): p. 237-244.
18. Gardon, R. and J.C. Akfirat, *Heat Transfer Characteristics of Impinging Two-Dimensional Air Jets.* Journal of Heat Transfer, 1966. **88**(1): p. 101-107.
19. Hadziabdic, M. and K. Hanjalic, *Vortical structures and heat transfer in a round impinging jet.* Journal of Fluid Mechanics, 2008. **596**: p. 221-260.
20. Popiel, C.O. and O. Trass, *Visualization of a free and impinging round jet.* Experimental Thermal and Fluid Science, 1991. **4**: p. 253-264.
21. Carlomagno, G.M. and A. Ianiro, *Thermo-fluid-dynamics of submerged jets impinging at short nozzle-to-plate distance: A review.* Experimental thermal and fluid science, 2014. **58**(0): p. 15-35.
22. El-Hassan, M., et al., *Experimental investigation of the wall shear stress and the vortex dynamics in a circular impinging jet.* Experiments in Fluids, 2012. **52**(6): p. 1475-1489.
23. Hall, J.W. and D. Ewing, *On the dynamics of the large-scale structures in round impinging jets.* Journal of Fluid Mechanics, 2006. **555**: p. 439-458.
24. Kataoka, K., et al., *Mass transfer between a plane surface and an impinging turbulent jet: the influence of surface-pressure fluctuations.* Journal of Fluid Mechanics, 1982. **119**: p. 91-105.
25. Alekseenko, S.V. and D.M. Markovich, *Electrodiffusion diagnostics of wall shear stresses in impinging jet.* Journal of Applied Electrochemistry, 1994. **24**: p. 626-631.
26. Phares, D.J., G.T. Smedley, and R.C. Flagan, *The wall shear stress produced by the normal impingement of a jet on a flat surface.* Journal of Fluid Mechanics, 2000. **418**: p. 351-375.
27. Kristiawan, M., et al., *Wall shear rates and mass transfer in impinging jets: Comparison of circular convergent and cross-shaped orifice nozzles.* International Journal of Heat and Mass Transfer, 2012. **55**: p. 282–293.
28. Meslem, A., et al., *Flow dynamics and mass transfer in impinging circular jet at low Reynolds number. Comparison of convergent and orifice nozzles.* International Journal of Heat and Mass Transfer, 2013. **67**(0): p. 25-45.
29. Bolashikov, Z., et al., *Improved inhaled air quality at reduced ventilation rate by control of airflow interaction at the breathing zone with lobed jets.* HVAC&R Research, 2013. **20**(2): p. 238-250.
30. Reiss, L.P. and T.J. Hanratty, *Measurement of instantaneous rates of mass transfer to a small sink on a wall.* AIChE Journal, 1962. **8**(2): p. 245–247.
31. Scarano, F., L. Riethmuller M, and J. Adrian R, *Advances in iterative multigrid PIV image processing.* Experiments in Fluids, 2000. **29**(3): p. S51-S60.
32. Westerweel, J., *Theoretical analysis of the measurement precision in particle image velocimetry.* Experiments in Fluids, 2000. **29**(1): p. S003-S012.
33. Nastase, I., A. Meslem, and M. El-Hassan, *Image processing analysis of vortex dynamics of lobed jets from three-dimensional diffusers.* Fluid Dynamics Research, 2011. **43**(6): p. 065502.
34. Baydar, E. and Y. Ozmen, *An experimental investigation on flow structures of confined and unconfined impinging air jets.* Heat Mass Transfer, 2006. **42**: p. 338–346.
35. Glauert, M.B., *The wall jet.* Journal of Fluid Mechanics, 1956. **1**(06): p. 625-643.
36. Tummers, M.J., J. Jacobse, and S.G.J. Voorbrood, *Turbulent flow in the near field of a round impinging jet.* international Journal of Heat and Mass Transfer, 2011. **54**(23–24): p. 4939-4948.

37. Xu, Z. and H. Hangan, *Scale, boundary and inlet condition effects on impinging jets.* Journal of Wind Engineering and Industrial Aerodynamics, 2008. **96**(12): p. 2383-2402.
38. Sengupta, A. and P.P. Sarkar, *Experimental measurement and numerical simulation of an impinging jet with application to thunderstorm microburst winds.* Journal of Wind Engineering and Industrial Aerodynamics, 2008. **96**(3): p. 345-365.
39. Vallis, E.A., M.A. Patrick, and A.A. Wragg. *Techniques of wall measurements in fluid mechanics*. In *Euromech.90.* 1977. Nancy, France.
40. Angioletti, M., et al., *Simultaneous visualization of flow field and evaluation of local heat transfer by transitional impinging jets.* International Journal of Heat and Mass Transfer, 2003. **46**(10): p. 1703-1713.
41. Lee, J. and S.-J. Lee, *The effect of nozzle aspect ratio on stagnation region heat transfer characteristics of elliptic impinging jet.* international Journal of Heat and Mass Transfer, 2000. **43**(4): p. 555-575.
42. Colucci D, W. and R. Viskanta, *Effect of nozzle geometry on local convective heat transfer to a confined impinging air jet.* Experimental Thermal and Fluid Science, 1996. **13**(1): p. 71-80.
43. Nastase, I., A. Meslem, and P. Gervais, *Primary and secondary vortical structures contribution in the entrainement of low Reynolds number jet flows.* Experiments in Fluids, 2008. **44**(6): p. 1027-1033.
44. El-Hassan, M. and A. Meslem, *Time-resolved stereoscopic PIV investigation of the entrainement in the near-field of circular and daisy-shaped orifice jets.* Physics of Fluids, 2010. **22**(035107): p. 26 p.
45. Ball, C.G., H. Fellouah, and A. Pollard, *The flow field in turbulent round free jets.* Progress in Aerospace Sciences, 2012. **50**: p. 1–26.
46. Todde, V., P.G. Spazzini, and M. Sandberg, *Experimental analysis of low-Reynolds number free jets. Evolution along the jet centerline and Reynolds number effects.* Experiments in Fluids, 2009. **47**: p. 279–294.